

# Surface Deformation and Shallow Dike Intrusion Processes at Inyo Craters, Long Valley, California

LARRY G. MASTIN AND DAVID D. POLLARD

*Department of Applied Earth Sciences, Stanford University, Stanford, California*

The Inyo craters are the two largest of four phreatic craters that lie within a 2.5-km-long, 500- to 700-m-wide N-S trend of faults and fissures at the south end of the Inyo volcanic chain in eastern California. The alignment of these features with dike-fed silicic volcanic centers of the same age a few kilometers to the north suggests that they were produced during intrusion of a dike at about 650-550 yr B.P. E-W extension south of south Inyo crater is ten to several tens of meters, suggesting that the dike is at least that thick. To understand how the faults and fissures developed, we mapped and studied the fault and fissure pattern; used a theoretical boundary element model to determine the surface strain profile above a shallow dike in a purely elastic medium; and conducted physical model experiments of fault and fissure growth. Results of the field studies and experiments indicate that deformation develops according to the following sequence: 1) extension fractures and perhaps other inelastic deformation develop immediately above the dike top and on the limbs of a shallow syncline which forms above the dike; 2) fissures form along two parallel trends at the surface on opposite sides of the dike plane, leaving a relatively unfractured region in between; 3) dip-slip movement on subsurface fractures, and linkage of these fractures with surface fissures produces inward-facing normal fault scarps that bound a nested graben above the dike. Experimental graben widths are up to several times narrower than predicted from the locations of theoretical strain maxima above a dilating crack in a linearly elastic medium. This fact is apparently due to the growth of a zone of inelastic deformation above the experimental dike top in the subsurface. If the ratio between the depth to the dike top and the distance between the outermost surface fissures at Inyo craters is within the range of ratios measured experimentally, then the depth to the dike top is between 250 m and several times that. A slant hole drilled in the summer of 1987 by the Department of Energy, Office of Basic Energy Sciences, intersected three breccia bodies of possibly intrusive origin directly below the center of south Inyo crater between 550 m and 610 m below the crater rim. No intact juvenile igneous rock was intersected, suggesting that the hole passed above the (magma-filled) dike top, perhaps passing through the zone of inelastic deformation which is inferred to exist from our model results.

## INTRODUCTION

The Inyo craters lie at the south end of the Inyo volcanic chain in eastern California. The Inyo chain represents one of the youngest volcanic features in an area of recent, active volcanism that includes the Long Valley caldera and the Mono Craters volcanic chain. With the exception of the Cascades Range, the Long Valley-Mono-Inyo area has exhibited more recent volcanic activity than any other area in the conterminous United States [Hill *et al.*, 1985]. Since the late 1970s, thousands of small earthquakes and ground uplift of >500 mm in Long Valley [Savage and Clark, 1982; Castle *et al.*, 1984] have raised concern that the magmatic system in the Long Valley area is active and capable of producing future eruptions.

Several studies [Pollard *et al.*, 1984; Fink, 1985; Miller, 1985; Eichelberger *et al.*, 1985] have proposed that the most recent eruptions in the Inyo chain were fed by one or more dikes. The existence of one or more dikes beneath the chain is suggested in part by the north-south alignment of eruptive vents and associated fissures and faults. In the Inyo craters area, four aligned craters (the largest two of which are the Inyo craters) lie within a 2.5-km-long, 500- to 700-m-wide, north-south trending set of nested grabens and fissures. The pattern of faults and fissures is similar to that

observed over dikes in volcanic rift zones elsewhere [Sigurdsson, 1980; Pollard *et al.*, 1983; Murray and Pullen, 1984]. In this paper, field information, numerical elastic models, and physical model experiments are utilized to understand how the fissures and faults at Inyo craters might have developed and to study the relationship between characteristics of the surface deformation and the depth and size of the dike. This research was part of the predrilling study for the Continental Scientific Drilling project at Inyo craters [Eichelberger *et al.*, 1988].

## TECTONIC AND GEOLOGIC SETTING OF THE INYO CRATERS

Silicic volcanism in the Long Valley area began about 2 Ma [Metz and Mahood, 1985] and climaxed about 0.73 Ma with the eruption of more than 600 km<sup>3</sup> of rhyolitic pumice-fall and ash-flow deposits (the Bishop Tuff), and the subsidence of the Long Valley caldera [Bailey *et al.*, 1976]. Activity since the subsidence of the caldera has included eruption of aphyric rhyolite between 730 and 650 ka during resurgent doming of the caldera floor; eruption of porphyritic hornblende-biotite rhyolite from centers peripheral to the resurgent dome 500, 300, and 100 ka; and eruption of porphyritic hornblende-biotite rhyodacite from caldera ring fractures in the Mammoth Mountain area (Figure 1) between 200 ka and 50 ka. Basaltic rocks erupted between 200 and 60 ka in the west moat of the caldera [Bailey *et al.*, 1976; Huber and Rinehart, 1967], and are part of a more extensive set of mafic volcanic rocks that extend

Copyright 1988 by the American Geophysical Union.

Paper number 88JB03015  
0148-0227/88/88JB-03015\$05.00

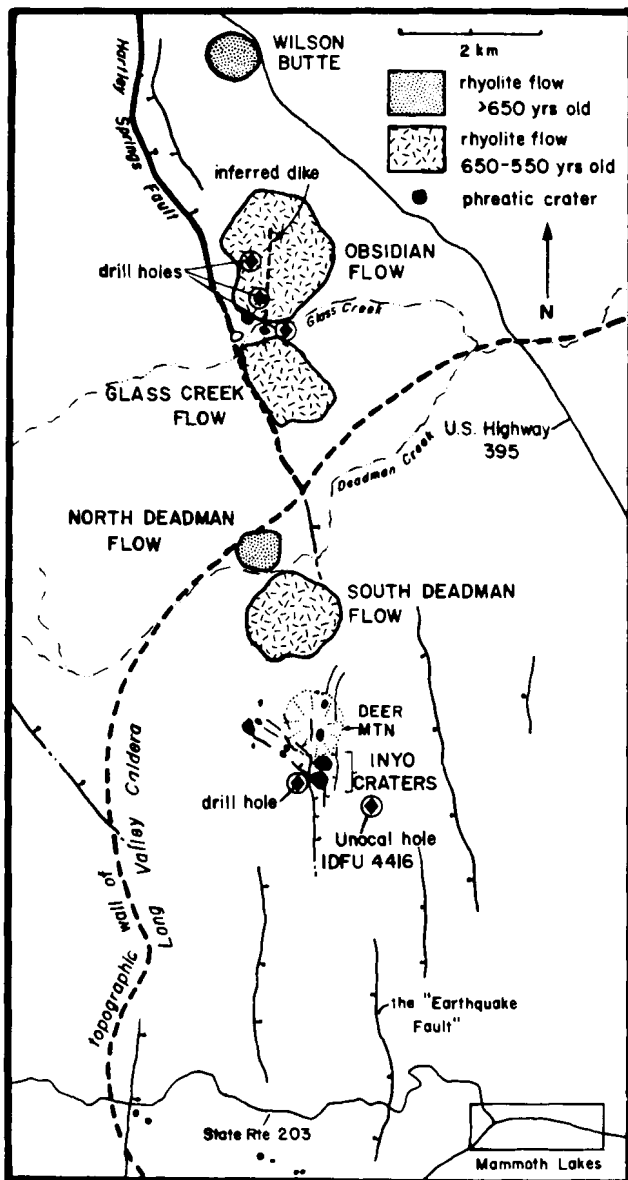


Fig. 1. Index map of Inyo volcanic chain. The circled diamonds are the sites of holes drilled by the Inyo Domes Drilling Project [Eichelberger *et al.*, 1985] to study the most recent Inyo chain volcanic features.

from southwest of Mammoth Mountain through the west moat of the caldera and 45 km northward. The composition of rocks in this trend varies from alkali andesite to alkali basalt, but for simplicity they are all referred to in this paper as basalt.

During the Holocene, most volcanic activity has been concentrated within a linear, north-south-trending region that crosses the northwest topographic wall of the Long Valley caldera, and includes the Inyo volcanic chain in the south and the Mono Craters in the north. The Inyo chain lies within a north-south-trending set of normal faults and extensional fissures that crosses the Sierra Nevada escarpment. Pre-Inyo eruptive vents (solid triangles, Figure 2) along the Inyo chain include Deer Mountain, a 180-m-high, steep-sided, 115-ka dome of pumiceous rhyolite north of Inyo craters [Bailey *et al.*, 1976] (Figure 1); at least two vents of

approximately 100-ka basaltic rock 750 m south-southeast and 1300 m north-northeast, respectively, of south Inyo crater; and a buried crater 900 m south-southwest of south Inyo crater.

North Deadman flow and Wilson Butte (Figure 1), which erupted about 6,000 and 1,200 yr B.P., respectively [Miller, 1985], are the oldest vents considered to belong to the Inyo chain. All other vents in the Inyo chain erupted during a relatively short time about 650-550 yr B.P. [Miller, 1985]. During this episode of activity, sub-Plinian eruptions from the Obsidian flow, Glass Creek flow, and South Deadman flow vents (Figure 1) produced thick blankets of near-vent pyroclastic fall, flow, and surge deposits. Lobes of ash covered more than 140 km<sup>2</sup> [Miller, 1985] and deposited about 1 m of ash at Inyo craters. After explosive eruptions ended, rhyolite lava was extruded from each of the three vents to form steep-sided, rubbly, sub-circular flows 1.0 to 1.8 km in diameter and more than 100 m thick in places. In the Inyo craters area, phreatic eruptive deposits overlie the deposits of the Obsidian, Glass Creek, and South Deadman vents. However, <sup>14</sup>C dates and tree-ring counts of a log incorporated in the south Inyo crater phreatic deposits [Wood, 1977] yielded a <sup>14</sup>C age of 550±60 yr B.P. for the eruption. This age is also suggested by the fact that some trees growing in south Inyo crater are more than 400 years old [Rinehart and Huber, 1965].

In 1984, a 7-m-thick rhyolite dike, similar in age and composition to the extrusive lava of Obsidian flow, was intersected by a slant drill hole (Figure 1) between Glass Creek flow and Obsidian flow [Eichelberger *et al.*, 1985], confirming the hypothesis that one or more dikes fed the flows in the northern part of the chain. The dike was intersected in the subsurface directly beneath a trend that includes a phreatic crater and the inferred center of the Obsidian flow vent, suggesting a dike orientation of about N60°E (Figure 1). Evidence for a young dike beneath the southern part of the chain is expressed in the fault and fissure pattern around the Inyo craters. We have mapped and studied these faults and fissures in order to understand how they formed, and what they might tell us about the depth and size of a dike in this area.

#### MAPPING AND FIELD STUDIES

The Inyo volcanic chain lies at the north end of a set of north-south trending faults and fissures several kilometers wide (Figure 1) that extends from the Inyo craters area at least 30 km south into the Sierra Nevada Mountains. The spacing between individual features in this set varies from several hundred meters to a few kilometers. The faults and fissures in the Inyo craters area lie within this larger regional set, but the former are spaced a few tens to a few hundred meters apart and increase in abundance toward the craters. Their concentration around the craters, their location at the south end of the dike-fed Inyo volcanic chain, and the nested graben structure around the craters themselves suggests that the origin of these features is more closely related to the intrusion of a subsurface dike than to the extension that apparently produced the faults and fissures in the regional trend.

The Inyo craters are located on a broad elongate topographic rise about 50 m high and 2 km in east-west dimension by 3 km north-south (Figure 2). Lying on the

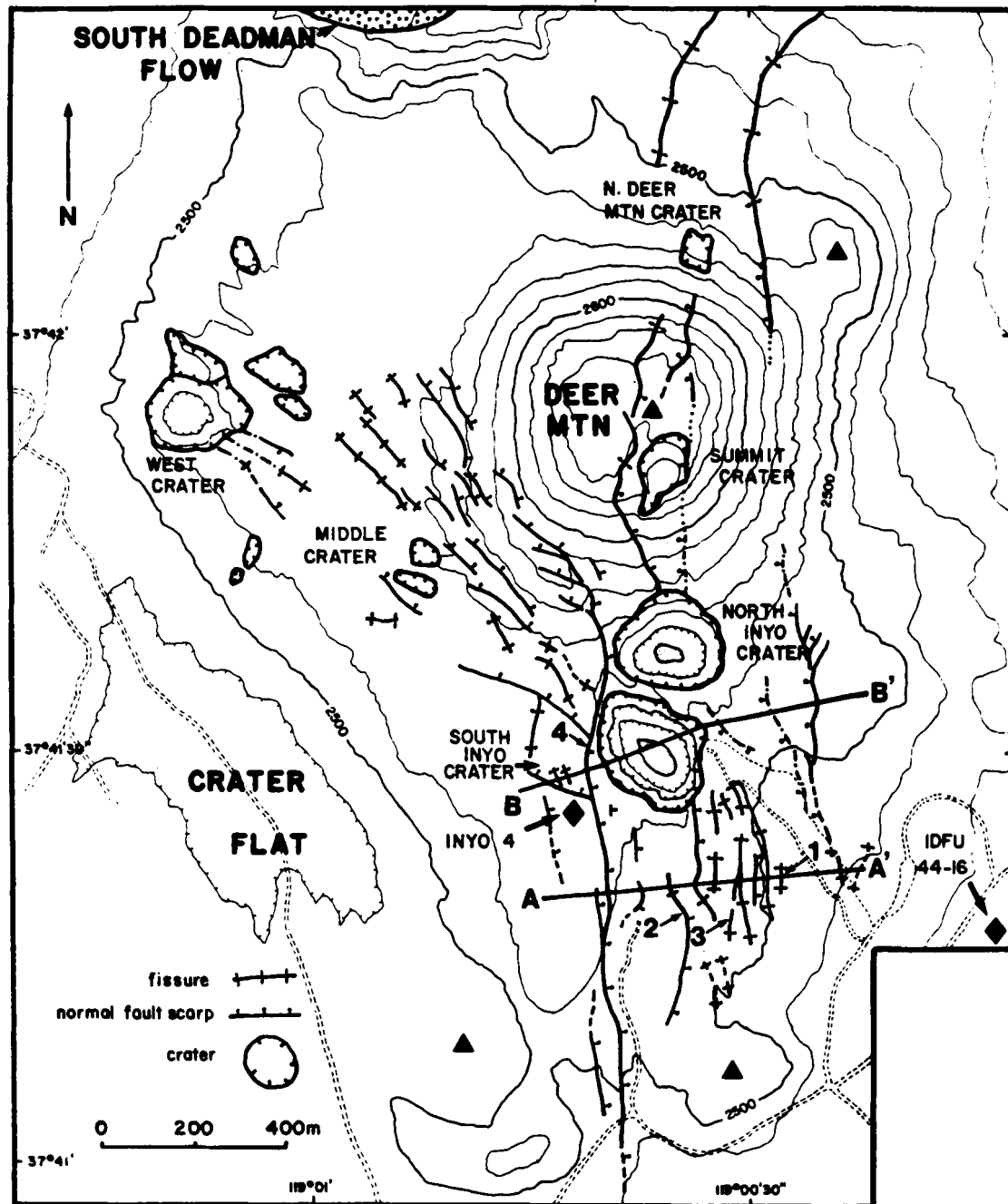


Fig. 2. Map of fissures and faults in the Inyo craters area. Fissure and faults are shown by solid lines where well defined, by dashed lines where poorly-defined or their existence is uncertain, by dot-dashed lines where mantled by phreatic debris, and by dotted lines where covered and totally obscured by phreatic debris.

east side of this high and dominating the topography for several kilometers in all directions is Deer Mountain. The north and south Inyo craters lie at the southern base of Deer Mountain, and two additional craters (referred to in this paper as "summit crater" and "north Deer Mountain crater") lie along a N-S trend near the top of the mountain and on the northern slope of the mountain, respectively.

A second set of craters, faults, and fissures trends northwest from the Inyo craters toward a prominent crater (referred to here as "west crater") about a kilometer away. This trend of features does not coincide with the main trend

of the Inyo chain and does not have a nested graben structure typical of surface deformation above shallow dikes. It is not clear from the surface evidence whether these features were produced by intrusion of a dike or by some other process. Therefore the northwest-trending features are not considered further in this paper.

Along the north-south trend, the normal fault scarps reach a maximum height of about 15 m on the west side of south Inyo crater (Figure 3, and Figure 2, location 4). South-southeast of south Inyo crater, numerous linear depressions a few tens of meters long, trending within about



Fig. 3. Photo looking south along fault scarp at location 4, Figure 2, immediately west of South Inyo Crater. The scarp has a nearly uniform slope from top to bottom of  $28^{\circ}$ - $30^{\circ}$ , and breaks in slope at the top and bottom that can be located to within about a meter. Blocks in the foreground, which were ejected from South Inyo Crater, pave the fault scarp in places. The height of the scarp here is about 15 m.

$20^{\circ}$  of north, are interpreted to be extensional fissures. These depressions are not drainage features as they are topographically closed at both ends and are usually filled with duff and pine cones rather than fluvial debris. Westward from the east end of section A-A' (Figure 2), these depressions change in form from subtle, v-shaped swales a few meters wide and about a meter deep to narrow, linear valleys several meters deep, with a spacing between them of a few to several tens of meters (Figure 4) containing dislodged and jumbled blocks of basalt. Exposures on the wall of south Inyo crater indicate that extension is accommodated in the subsurface by opening of pre-existing cooling cracks in the massive, cliff-forming basalt flow units (Figure 5, arrows). In the rubbly zones above and below the massive flows, a lack of distinct fissures suggests that the extension occurs diffusely throughout those units, perhaps by intergranular motion and shearing.

In profile A-A' (Figure 6) south of south Inyo crater, fissures and faults are concentrated in two zones on opposite sides of a N-S line through the center of south Inyo crater (which intersects A-A' at about 200 m horizontal distance in Figure 6), with a relatively unfractured region in between. The western zone of deformation is about 40 m wide and consists of two normal faults with a total down-to-the-east vertical displacement of about 15 m. The eastern zone of deformation is about 400 m wide and includes fissures and small grabens. No individual fault or fissure dominates the eastern zone, and apparently there is little net vertical displacement across the zone. In the vicinity of south Inyo crater (profile B-B', Figure 6), inward facing normal fault scarps are well developed on both sides of the crater but closely spaced fissures like those in the eastern zone of profile A-A' are absent. Some of the smaller closely-spaced features like those of the eastern zone in section A-A' may be obscured in B-B' by phreatic debris, which is several meters thick east of south Inyo crater.

At locations 2 and 3 (Figure 2), minimum opening

displacements of 3.7 and 2.5 m, respectively, were measured from split vesicles on the walls of each fissure to matching vesicles on blocks that had pulled away from the fissure walls and now lie near the center of each fissure. The



Fig. 4. Fissure southeast of South Inyo Crater (location 1, Figure 2). The fissure has opened by separation of cooling fractures in basalt. Total opening displacement at this point was measured as 2.7 m.



Fig. 5. A set of open cracks (arrows) in the basalt on the southwest wall of South Inyo Crater. Height of the cliff face is about 5 m.

locations of these blocks, near the center of the fissure rather than on the side of the fissure opposite the matching fissure wall, suggests that the total opening displacement in each fissure is considerably greater than the measured minimum. At location 1 (Figure 2; and Figure 4), a total opening of 2.7 m was measured between opposite walls of the fissure. Strike-slip displacement between matching points at each of these locations is small relative to opening displacement. The sum of these measured opening displacements gives a minimum opening displacement of 9.7 m across the area. To estimate the extension across A-A', we assume that the actual opening displacements at locs. 2 and 3 are twice the measured minima (i.e., 7.4 m and 5.0 m, respectively), and that the opening displacements on the unmeasured fissures in A-A' are equal to the average (5.0 m) of the measured fissures. In addition, we arbitrarily assume that the normal faults on the west side of A-A' range in dip between  $60^\circ$  and  $80^\circ$ . With these assumptions, the total opening across A-A' is approximately 40 m and the extension is approximately 6%. Given the uncertainty in these assumptions, the actual opening displacement could be a few tens of meters less than or greater than that estimated.

#### ANALYSIS

##### Theoretical Models

In order to relate the surface deformation to the depth, size, and orientation of the inferred dike, we compare the

fault and fissure pattern at Inyo craters with the theoretical strain profile above a shallow, pressurized crack (i.e. a dike) in an elastic half-space. The elastic strain profile is calculated using a boundary element method similar to that employed elsewhere [Pollard *et al.*, 1983; Rubin and Pollard, 1988] to model surface deformation above shallow dikes. This theoretical approach is useful for studying the state of elastic deformation around a dike before other inelastic structures, such as fissures and faults, form. Inelastic deformation, which may modify the strain and stress fields significantly, is considered later in this paper.

The boundary element method [Pollard and Holzhausen, 1979; Crouch and Starfield, 1983] solves for the stresses, strains, and displacements in a homogeneous, isotropic, linearly elastic body by dividing the boundaries of the body into discrete segments (Figure 7). Imaginary normal ( $\sigma_n$ ) and shear ( $\sigma_s$ ) stresses are applied to each boundary element such that the sum of these imaginary stresses, plus the stresses imposed on each element by all other boundary elements and by the regional stresses, equals the specified boundary conditions.

We approximate the dike as a planar, pressurized crack of some arbitrary orientation and height  $h$  from top to bottom (Figure 7). The resulting strains are a function of the geometry of the crack and the pressure distribution inside it, whether the pressure be exerted by magma, steam, breccia, or some combination of these materials. The location of the magma chamber that fed the Inyo volcanic chain is uncertain; however, seismic and geodetic data [e.g. Hill *et al.*, 1985] indicate that if it still exists, it lies at least a several kilometers below the surface. Therefore in our analysis we choose a dike whose bottom is very deep (more than 10 km) relative to the depth of its top (50 to 400 m). Along the walls of the dike, the boundary conditions are zero shear stress and a compressive normal stress equal to the driving pressure  $P_d(y)$ . This driving pressure is the difference between the pressure within the dike  $P_m(y)$  and the compressive normal stress  $S_h(y)$  that acted across the

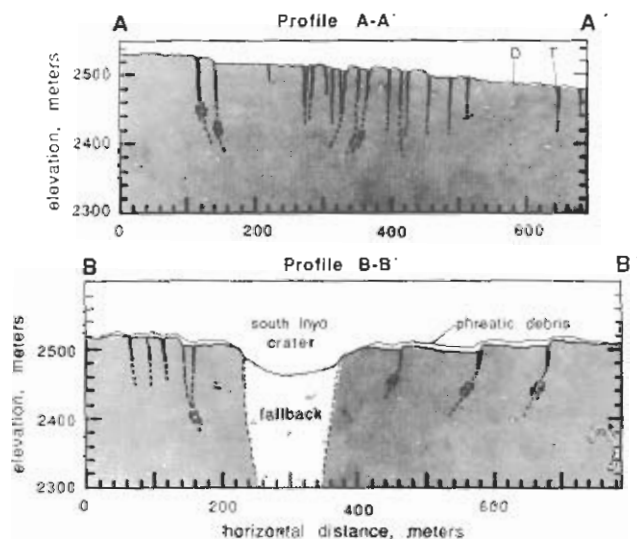


Fig. 6. Two profiles, along lines A-A' and B-B' in Figure 2. Letters "D" and "T" in profile A-A' denote the locations of the dirt road and trail, respectively, mapped in Fig. 2. Subsurface fissure and fault patterns are schematic and are based on experimentally produced patterns of fissures and faults.

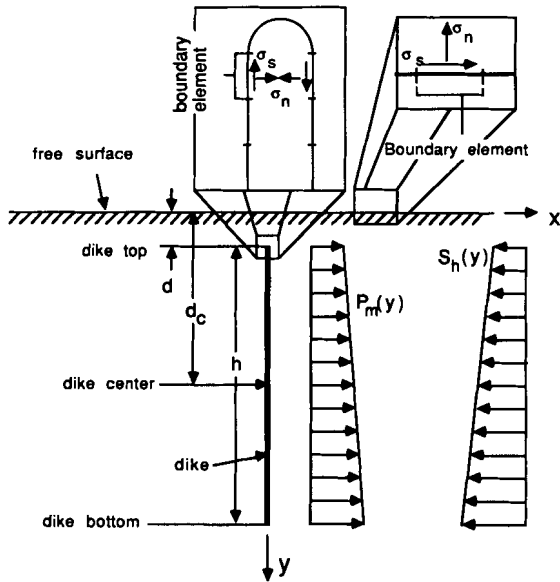


Fig. 7. Illustration of some of the features included in the boundary element program to determine the strain profile above a shallow dike.  $P_m(y)$  is the pressure in the dike, which is a function of depth  $y$ .  $S_h(y)$  is the regional normal stress perpendicular to the dike walls.

dike plane before dike emplacement (Figure 7). The driving pressure may have been uniform over the height of the dike, but more likely it increased or decreased with depth  $y$ .

Given these conditions, the theoretical horizontal strain at the free surface has the form of two maxima located on opposite sides of the dike plane (Figure 8). For a given driving pressure distribution, the locations of the elastic strain maxima are independent of dike thickness. The magnitude of the horizontal strain, however, is proportional to the thickness of the dike. Therefore, the elastic strain values in Figures 8 through 10 are given in strain per meter average dike thickness. Pollard *et al.* [1983] found that above dikes of moderate height  $h$  relative to their depth  $d$ ,

the distance  $s_e$  between the maxima is 2-3 times the dike depth  $d$ . For  $h \gg d$ , we find that the ratio  $s_e/d$  ranges narrowly between 2.8 and 3.0. These results suggest that fissures and faults related to extension should be concentrated in two zones on opposite sides of the dike plane, with a zone of lesser deformation in between. These two zones of deformation should be closer together above a shallow dike than above a deeper one.

The fissures and faults south of south Inyo crater are confined to a zone no more than 670 m wide. If the width of the zone of surface deformation in this area corresponds to the spacing of elastic strain maxima above a vertical dike, the theoretical range  $s_e/d$  constrains the depth of the dike top to be less than about 250 m. If the spacing of about 260 m between the centers of deformation in profile A-A' corresponds to  $s_e$ , the dike top would be approximately 100 m deep.

Previous studies have not considered the effect of variations in driving pressure distribution on the surface strain profile. We find that for a given dike depth, the ratio  $s_e/d$  varies by less than a few percent regardless of whether the driving pressure in the dike increases linearly, decreases linearly, or is constant with depth (Figure 9). The magnitude of the extension at the surface above the dike, however, varies considerably. For example, for a vertical dike with a top at 100 m depth and with a driving pressure that decreases linearly downward to zero at its bottom (case 1, Figure 9), the extension across a 700-m-long profile above the dike (such as A-A', Figure 6) would be 0.41 m per meter of dike thickness. For the same case with a linearly upward decreasing driving pressure (case 3, Figure 9), the extension across A-A' would be 0.22 m per meter of dike thickness. Recalling that the surface extension along profile A-A' ranges from at least 10 m to possibly several tens of meters, the values given above suggest a dike thickness that ranges from a few tens to a few hundred meters.

Decreasing the dip of the dike from  $90^\circ$  makes the extensional strain peak broader and higher on the hanging wall side than the footwall side (Figure 10), suggesting that

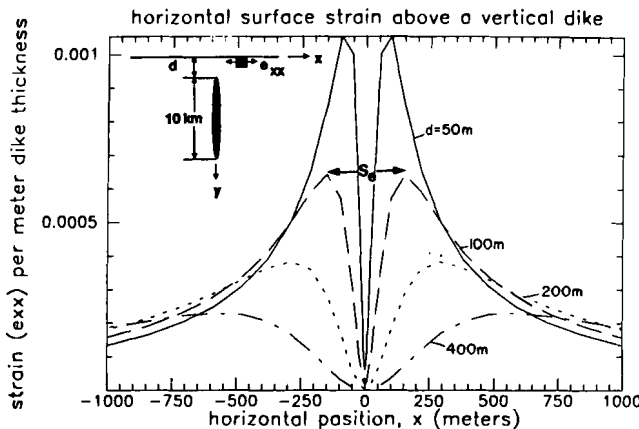


Fig. 8. Horizontal extensional strain ( $e_{xx}$ ) parallel to the Earth's surface per meter average dike thickness, versus horizontal position  $x$  measured from the point immediately above the dike, in a direction perpendicular to the dike plane. Curves are for  $d=50$  m (solid curve), 100 m (long-dashed curve), 200 m (short-dashed curve), and 400 m (long-dashed, short-dashed curve). A uniform driving pressure along the dike length is assumed in all models.

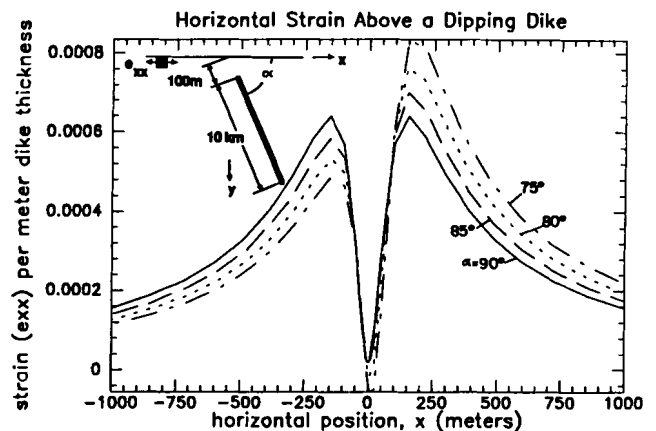


Fig. 9. Horizontal surface strain per meter dike width under three different driving pressure distributions. Case 1, (solid curve) linear upward increase in driving pressure with a driving pressure of zero at the bottom of the dike. Case 2, (long-dashed curve) uniform driving pressure. Case 3 (short-dashed curve) linear upward decrease in driving pressure with a driving pressure of zero at the dike top.

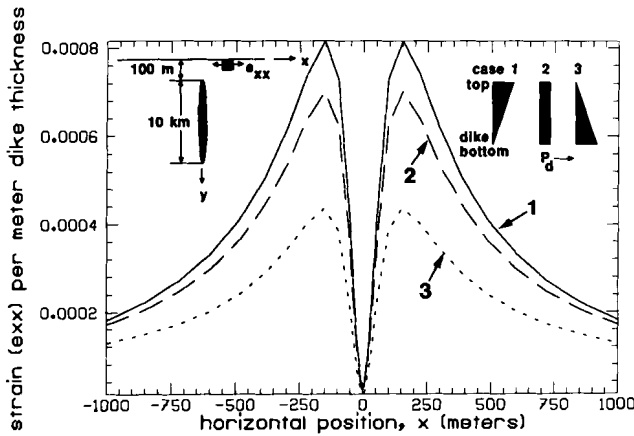


Fig. 10. Horizontal strain per meter average dike width for dikes at 100 m depth, dipping  $90^\circ$  (solid curve),  $85^\circ$  (long-dashed curve),  $80^\circ$  (short-dashed curve), and  $75^\circ$  (long-dashed, short-dashed curve). Horizontal distance is measured from the point where the dike plane intersects the surface.

the zone of fissuring may be wider, and extensional strain may be greater, above the hanging wall side of the dike. The asymmetric distribution of faults and fissures in profile A-A' (Figure 6) and the fact that the Inyo craters lie toward the west side of the zone of deformation (Figure 2) suggest that the dike may dip eastward beneath the craters. Theoretical strain profiles are consistent with the relative widths and locations of the regions of deformation in profile A-A' for dike dips ranging from  $90^\circ$  to about  $70^\circ$ . The asymmetric pattern of surface deformation could also have been produced by variations in material properties of the host rock or by inelastic processes not considered in this model.

#### Physical Models

The theoretical analysis does not explicitly include faults and fissures, which probably developed during a complex process, each stage of which was influenced by the stage that preceded it. To study this process, physical model experiments were conducted to simulate dike intrusion. A weak granular solid, consisting of a mixture of all-purpose flour and white granulated sugar, in a sugar to flour ratio of 3:1 by volume, was packed and, in some experiments, layered with corn meal in a small box with plexiglass panels on the front and back (Figure 11). The corn meal layers served primarily as marker beds, although they also may have been the sites where extensional fractures first formed. Cardboard sheets were inserted through a slit in the bottom of the box to dilate a sleeve consisting of two sheets of linoleum, taped together at the top. During dilation of the sleeve, the outward displacement of the flour-sugar mixture was accommodated at the ends of the box by cushions of polyurethane foam. Friction between the host material and the bottom of the box was eliminated by having the host material ride atop linoleum sheets that were pushed outward by the cardboard inserts.

Hubbert [1937], among others, outlined the mathematical criteria by which the physical properties of model materials are scaled to preserve mechanical similarity with the prototype (i.e. with the system being studied). Hubbert pointed out, for example, that a decrease in the

length scale of a physical model relative to the prototype generally requires a proportional decrease in strength of the model material to maintain mechanical similarity. Ideally, other mechanical properties including elastic moduli and magnitudes of surface and body forces in the physical model must be scaled to maintain strict mechanical similarity. Lack of knowledge of these properties in the Earth, however, and the limitations imposed by the properties of materials at hand have prevented strict scaling of most experiments to date. Thus most studies (including those by Cloos [1939], Cloos [1955, 1968], Oertel [1965] and Horsfield [1977, 1980]) have been only loosely scaled with respect to strength by changing the properties of the model material until the features produced in the experiments are similar in appearance to the geologic features being studied. Similarly, in this study, the relative proportions of flour and sugar have been adjusted until the pattern of surface deformation resembles that at Inyo craters. This approach does not necessarily insure that the sequence of deformation in the physical models is similar in all respects to that at Inyo craters, but it provides a possible model for deformation that can be studied by direct observation.

About 60 experiments were run in which (1) patterns of fissures and faults were photographed at successive stages of growth, (2) the sequence of fault and fissure development was mapped at the surface, (3) extensional strain profiles across the surface were measured at successive stages of growth, and (4) the distance between faults and fissures was measured and plotted as a function of depth to the top of the linoleum sleeve. To measure extensional strain, markers were placed 8-9 mm apart along two rows perpendicular to the plane of the sleeve. Changes in the distance between the markers were measured using a microscope with a micrometer graticule in the eyepiece. Relative displacements could be resolved to within approximately 0.03 mm, giving a strain resolution of about 0.3%.

*Sequence, magnitude, and style of deformation.* The sequence of fault and fissure growth is illustrated in photographs in Figure 12. In all cases fissures become visible when dilation of the linoleum sleeve approaches 0.08-0.10 times the sleeve depth  $d$ . As predicted by the

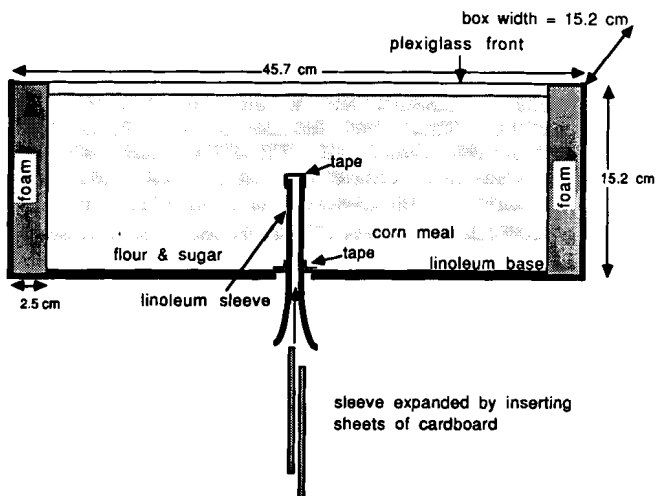


Fig. 11. Illustration of box used for physical models of deformation associated with dike emplacement. The dimensions of the box are 45.7 cm long, 15.2 cm wide, and 15.2 cm deep.



theory, the fissures are concentrated in two regions on opposite sides of the plane of the sleeve (e.g. locations A and B, Figure 12a). The number of fissures and the average width of the zones of fissuring on opposite sides of the centerline are generally though not always similar. The overall trends of most fissures are roughly parallel to the trend of the linoleum sleeve, though sections of individual fissures up to a few millimeters long vary by more than  $60^\circ$  from this orientation (location B, Figure 12a). Branched fissures may form when a younger fissure abuts against an older fissure (location C, Figure 12b).

The growth of fissures on opposite sides of the sleeve is accompanied by the development of a shallow topographic trough a few millimeters deep immediately above the sleeve top, flanked by two gentle topographic highs located outboard of the fissure zones (illustrated by the horizontal black line locating the original surface elevation in Figures 13a-13c). Fissures grow on the inner slopes of the two flanking ridges, and younger fissures tend to form progressively inward toward the plane of the sleeve relative to the older ones. During fissure growth, narrow asymmetric ridges that appear to be the surface expressions of small thrust faults (location D, Figure 12c) form between the innermost fissures.

When the maximum dilation of the linoleum sleeve approaches about  $0.2d$ , dip-slip movement produces monoclines (location E, Figure 12c) and a graben bounded by inward facing vertical normal fault scarps (location F, Figure 12c). At the base and top of well-developed fault scarps like the one at location F, Figure 12c, the surfaces have been tilted back to a horizontal orientation, effectively unbending part of the downwarped trough above the sleeve top. In some cases the unbending is accompanied by growth of small extensional fissures within the graben.

As fissures form at the surface (location a, Figure 13a), indistinct vertical fractures and zones of disaggregation develop in the subsurface around the sleeve top (location b, Figure 13a) and on the limbs of a syncline that underlies the central trough. Extension immediately above the sleeve top is clearly too great to be accommodated by the opening of the visible extension fractures in the corn meal alone, suggesting that the region above the sleeve is pervasively sheared. On the limbs of the syncline, subsurface extensional fractures develop (locations c and d, Figure 13b), begin to accommodate dip slip movement, and propagate by connecting with extensional features in adjacent layers (e.g., location e, Figure 13c) and with fissures at the surface (location f, Figure 13c) to form normal fault scarps. Because they form from nearly vertical surface fissures, the normal faults are vertical to steeply dipping at the surface, but they can range in dip down to about  $70^\circ$  at depth. Near the base of the normal faults, dip-slip displacement becomes distributed within a relatively diffuse zone of shearing and extension along the limbs of the syncline above the sleeve top.

In experiments where corn meal is not layered with the flour-sugar mixture, no subsurface extensional fractures are observed, possibly because the flour is smeared against the plexiglass walls. However, the pattern and the sequence of surface deformation are identical to those in the layered experiments, suggesting that the mechanism of normal fault development is also the same.

Measured profiles of horizontal extensional strain during

fissure and fault growth (Figure 14) have some characteristics of theoretical strain distributions but are also influenced by inelastic processes. In particular, all profiles show regions of high extensional strain on opposite sides of the centerline, with an extensional strain minimum at the centerline. Comparison of the left side of stage 2 with that of stage 1 clearly indicates that the first fissure (arrow labeled "nc" for "new crack") forms in the area where the extensional strain in stage 1 before fissuring was greatest. However, the distance between the regions of greatest measured strain in stage 2 is about one half to two thirds the distance  $s_e$  between the maxima in the theoretical strain profile (solid line, stage 2) obtained from a boundary element model of this experimental setup (the appendix). In addition, although the theoretical strain profile is continuous, the measured strain profile is relatively discontinuous; most extension occurs by dilation of fissures.

An additional discrepancy between the theoretical and experimental results involves the growth of large contractional strains immediately above the sleeve top at the surface in the experiments. Contractional strains develop simultaneously with the growth of fissures on opposite sides of the sleeve plane (stage 2). They reach a maximum when normal faults ("nf," stage 4) first appear and decrease (stage 5) during the growth of the normal faults.

The ratio of measured extension at the surface to average sleeve width ( $t_a$ , Figure 14) is 0.59-0.73, which is considerably greater than the range 0.22-0.41 estimated from the elastic models.

*Relation between fissure zone width and sleeve depth.* Previous papers [Fink and Pollard, 1983; Pollard et al., 1983, 1984] suggest that the distance between the innermost fissures above the top of a dike of finite height ( $h$ , Figure 7) is roughly 2-3 times the depth to the dike top. This rule of thumb is based on the assumption that fissures will form at the surface where the theoretically determined elastic strain is greatest and ignores the effects of inelastic deformation in controlling the locations of surface fissures. In the experimental results it was found that surface fissures tend to grow progressively inward toward the plane of the linoleum sleeve even though the top of the sleeve is stationary. Thus the spacing of the innermost fissures is a poor indicator of sleeve depth.

The spacing between the outermost fissures, which are usually the first to form, is more likely to correlate with the spacing between peaks in the elastic strain profile. To study the relationship between the width of the deformation zone in our physical models and the depth  $d$  to the top of the linoleum sleeve, the spacing  $s_m$  between the outermost fissures at the surface was measured for  $d$  ranging from 9 to 67 mm in 32 experiments. Two sets of experiments were conducted. In one set (top, Figure 15a), a linoleum sleeve was dilated by inserting cardboard sheets as before, to a thickness of 15-19 mm. Measurements of  $s_m$  were made along 10-11 equally spaced surface profiles and average values of  $s_m$  for each experiment were plotted as a function of  $d$  (solid diamonds, Figure 15b). In the second set of experiments (bottom, Figure 15a), two stiff sheets of plywood, connected at the top by stretchable fabric (Figure 15a), were wedged apart. Measurements of  $s_m$  were made immediately after fissures formed (rather than after the sleeve had been dilated to a prescribed width as in the first



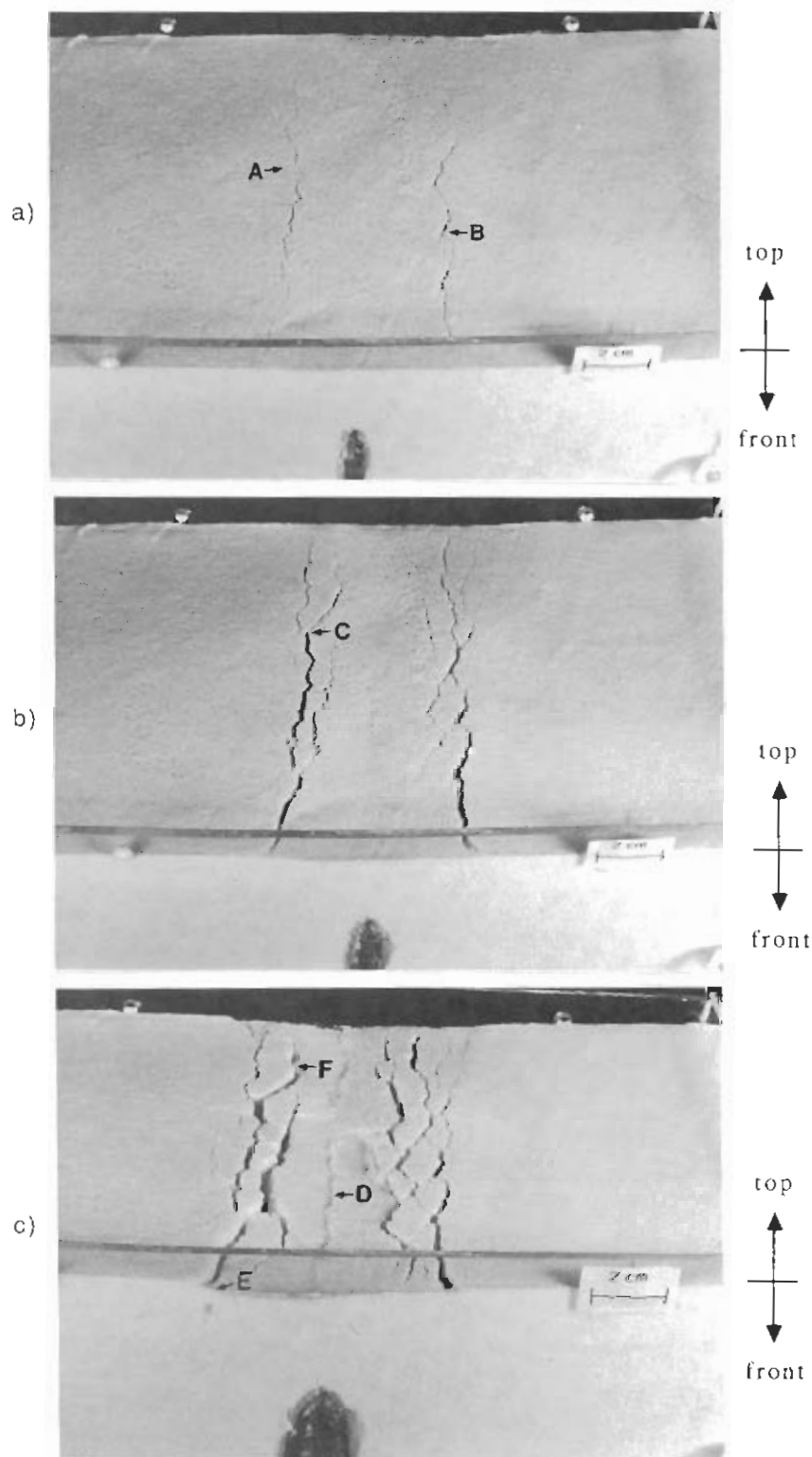


Fig. 12. Photographs of three stages of surface deformation during dike inflation. (a) Growth of a few small fissures (locations A and B) on opposite sides of the dike plane at the surface. (b) Growth of additional fissures (location C). (c) Growth of a pressure ridge immediately above the dike (location D) and development of dip slip movement along some of the innermost fissures to form inward facing normal fault scarps (locations E and F).

experiments), and average values of  $s_m$  were plotted as a function of  $d$  (solid circles, Figure 15b). Preliminary runs of the first set of experiments were performed using ratios of flour to sugar ranging from 1:20 to 1:1. It was found that the fissure spacing for a particular sleeve depth is

essentially independent of the flour:sugar ratio, even though the cohesion of the mixture changes considerably over this range.

The trend of  $s_m$  versus  $d$  does not extrapolate back to the origin for the first set of experiments (Figure 15), whereas it

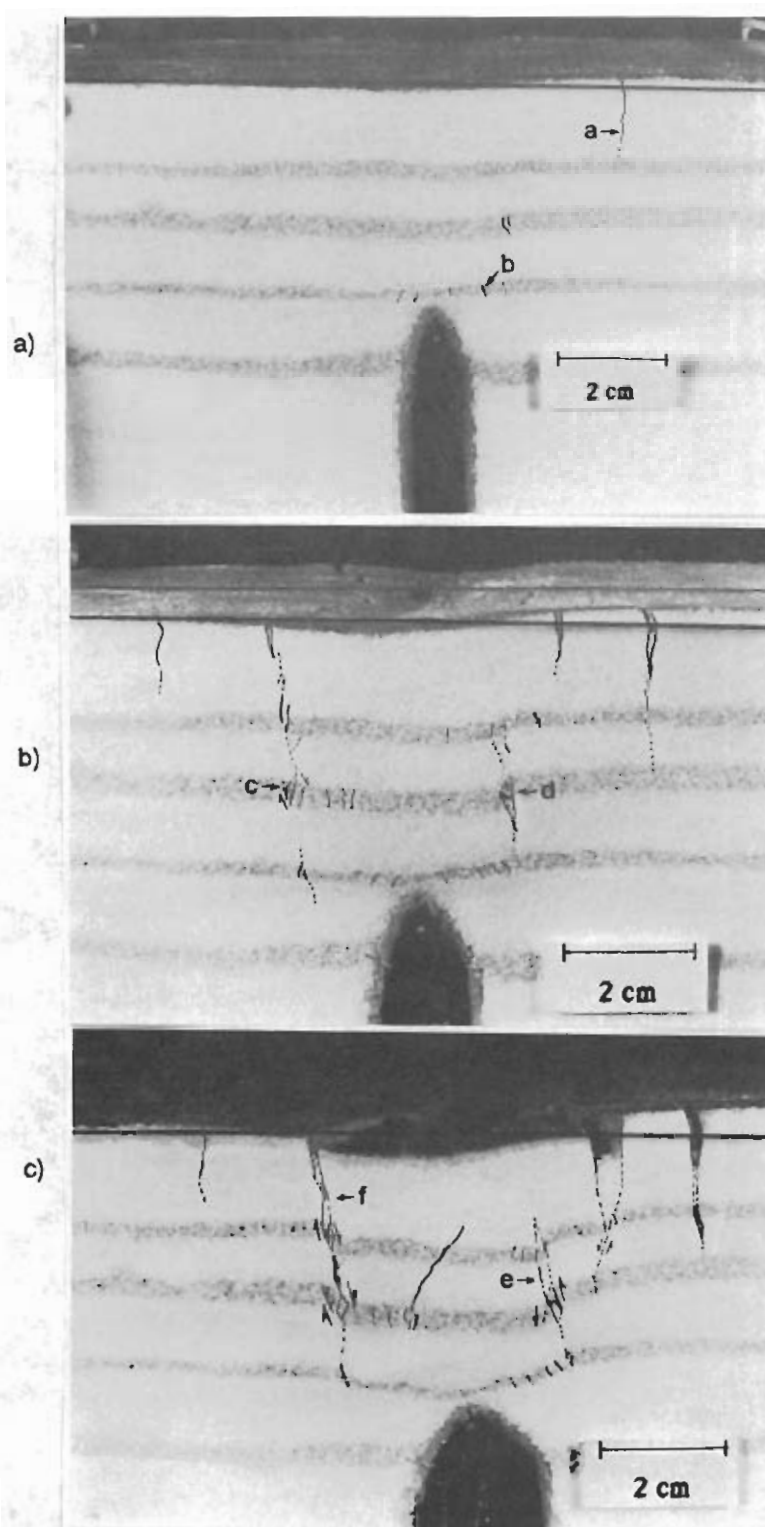


Fig. 13. Cross-sectional photographs of deformation. The dark layers are corn meal and the light layers consist of a 3:1 mixture by volume of granulated sugar and white flour. Obvious fractures (solid black vertical lines) and less obvious fractures (dashed lines) were mapped during the experiment. The black horizontal line represents the original location of the surface.

does (roughly) for the second set. This is partly due to the fact that in the first set of experiments, the sleeve continued to be dilated after the fissures formed. Thus fissures were physically translated away from the sleeve plane during further dilation, thereby increasing  $s_m$ . This effect is most significant for  $d$  less than about 40 mm. It is insignificant

for  $d$  greater than about 50 mm, where the sleeve had to be dilated to nearly its maximum thickness to produce the fissures.

Values of  $s_m$  are compared with theoretical predictions of  $s_e$  obtained from a boundary element model (the appendix) for the linoleum sleeve (shaded region) and the wedged

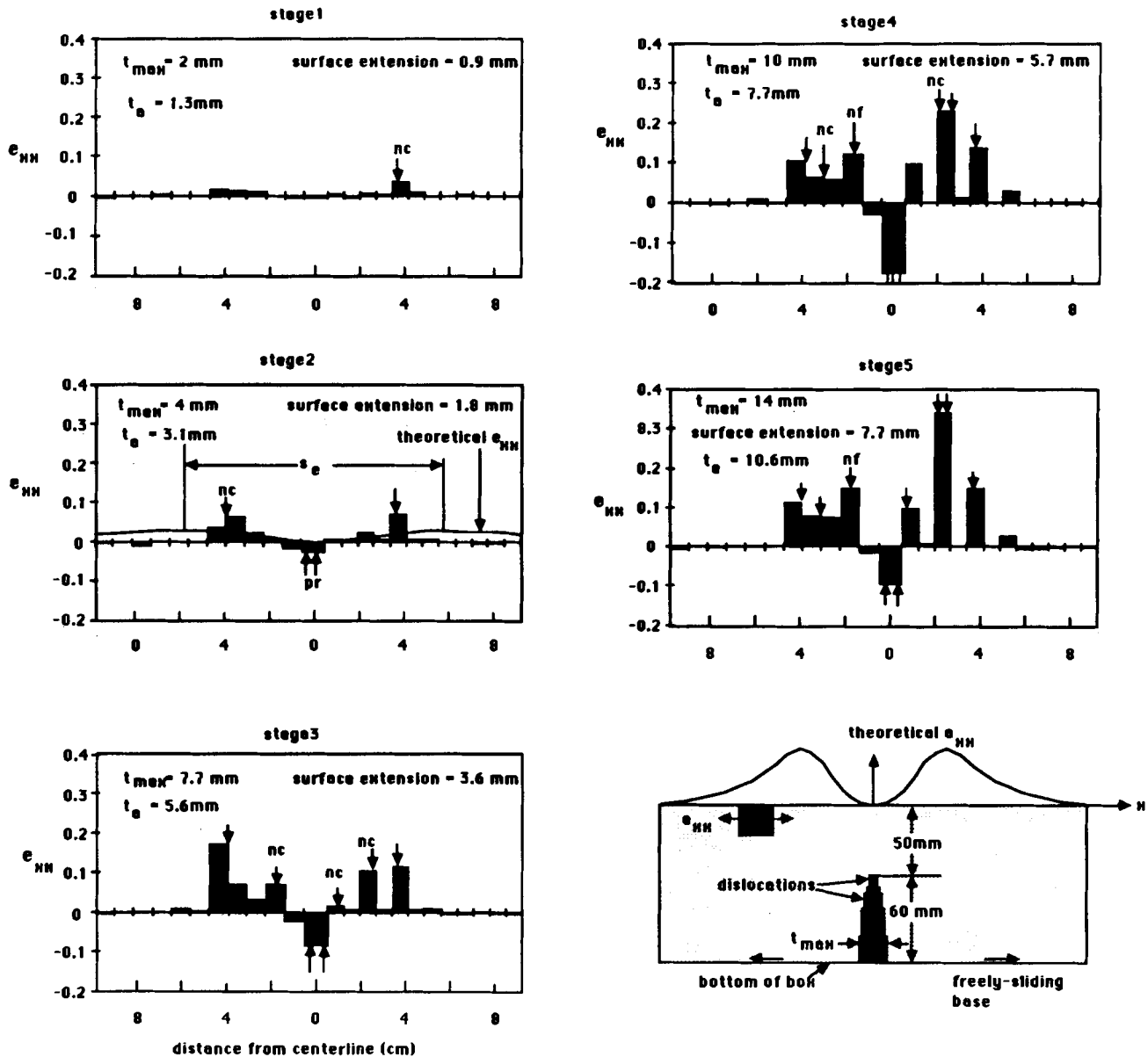


Fig. 14. Bar charts of measured horizontal extensional strain ( $e_{xx}$ ) at the surface of the physical model plotted versus horizontal distance from the centerline above the linoleum sleeve, at successive stages of dilation of the sleeve. Arrows represent the locations of (1) new fissures (labeled "nc"), (2) fissures which formed during a previous stage (unlabeled arrows above the  $e_{xx}=0$  axis), (3) normal faults ("nf"), (4) new pressure ridges ("pr") and pressure ridges which formed during a previous stage (unlabeled arrows below the  $e_{xx}=0$  axis). Lower right-hand corner: illustration of the dislocation configuration used to model the theoretical strain profile in stage 2.

plywood experiments (heavy solid curve). The experimental values of  $s_m$  agree with  $s_e$  only for small values of  $d$  in the first set of experiments. In the second set of experiments, average values of  $s_m$  range from about 17% to 53% of  $s_e$  throughout the range of depths.

#### DISCUSSION

These experimental results clearly are not predicted by the theory. Variations in boundary conditions caused by edge effects in the experimental box have been considered as a possible explanation (the appendix), but none gives the decrease in  $s_e$  required to explain the experimental data. We suggest that the discrepancy between the theoretical spacing

of strain maxima and the experimental spacing of outermost fissures is caused by inelastic deformation in the form of extensional fracturing and pervasive shearing at the top of the linoleum sleeve. Such zones of inelastic deformation ("process zones"), composed of dike-parallel joints, have been recognized near the tips of mafic dikes in sedimentary host rocks on the Colorado Plateau [Delaney *et al.*, 1986]. Other types of inelastic deformation, such as pervasive shearing or plastic yielding, may occur ahead of dike tips elsewhere [Pollard, 1988].

Irwin *et al.* [1958] showed that inelastic deformation in a process zone at the tip of a crack produces an elastic strain field beyond the process zone which is similar to that ahead of a longer crack in a purely elastic medium. In our

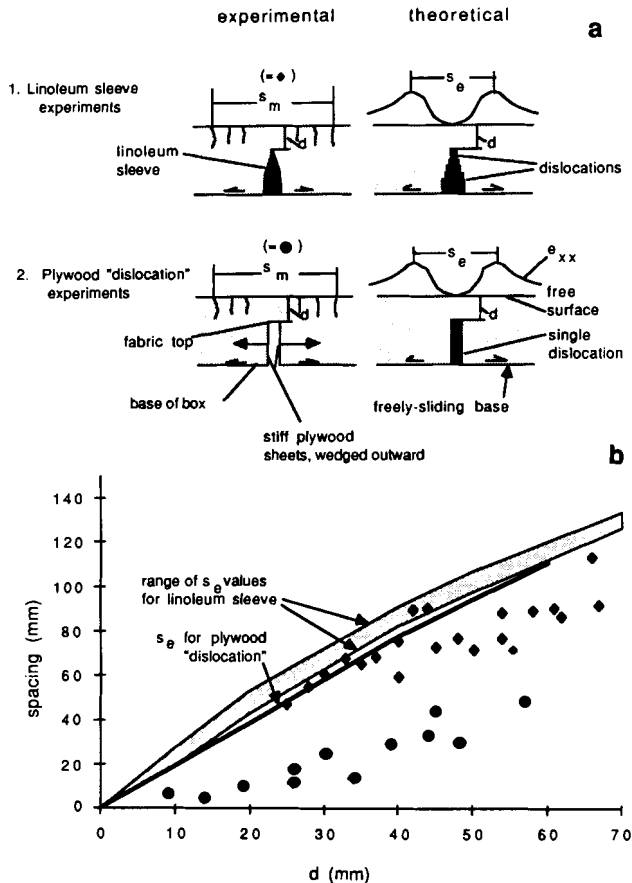


Fig. 15. Plot of the maximum spacing  $s_m$  between fissures in the physical models, as a function of dike depth. Diamonds denote average values of  $s_m$  in experiments in which a linoleum sleeve was dilated using cardboard sheets to approximate dike inflation. Solid circles represent average values of  $s_m$  for experiments in which dike inflation was approximated by wedging apart two parallel sheets of plywood. The range of theoretical values of the distance between elastic strain maxima ( $s_e$ ) for the linoleum sleeve experiments are shown by the shaded region. Theoretical values of  $s_e$  for the plywood experiments are shown by the heavy solid curve.

experiments, this effect explains why the measured strain maxima are closer together (as in Figure 14, stage 2) than the theory predicted. Because the positions of the strain maxima observed in Figure 14, stage 2, correspond approximately to the positions of the outermost fissures, the above explanation also accounts for the fact that  $s_m$  is less than  $s_e$  in Figure 15.

In theory, the size of the process zone beyond a crack tip depends on the driving pressure distribution in the crack [Broek, 1982, p. 92]. A driving pressure that is constant or decreases toward the crack tip produces a tapered crack profile, a lower tensile stress concentration, and a smaller process zone. A driving pressure which increases toward the crack tip produces a more box-shaped profile near the crack tip, a higher tensile stress beyond the tip, and a larger process zone. Thus, for two dikes of the same average thickness with tops at the same depth, a smaller value of  $s_m$  would be expected above a box-shaped dike tip than above a tapered dike tip. This relationship partly explains the lower values of  $s_m$  obtained for the plywood slot experiments than for the linoleum sleeve experiments at large values of  $d$ , as shown in Figure 15.

An increase in the average driving pressure in a crack produces an increase in the average opening displacement and tends to increase the size of the process zone [Broek, 1982, p. 92; Delaney *et al.*, 1986]. This fact may be used to explain why  $s_m$  does not approach  $s_e$  as  $d$  increases in Figure 15. If the size of the process zone were constant regardless of the dike depth, the process zone would be expected to become less important in determining the elastic strain profile at the surface as  $d$  increased, and  $s_m$  would approach  $s_e$  with increasing  $d$ . That this is not the case reflects the fact that the sleeve thickness required to produce fissures at the surface also increases with  $d$ . The increase in average sleeve thickness with depth is probably accompanied by an increase in the average size of the process zone, which in turn is probably responsible for the increase in the discrepancy between  $s_m$  and  $s_e$  with  $d$ .

The fact that new fissures tend to form on the inward sides of older ones in the experiments suggests that the top of the process zone migrates upward as the sleeve is dilated. Eventually, strain is accommodated at the surface by normal faulting rather than the growth of new fissures. This growth sequence suggests that the process zone does not simply grow vertically toward the free surface but extends along the limbs of the syncline above the sleeve. The growth of normal faults at the surface may represent the stage at which inelastic deformation propagates from the top of the sleeve to the surface.

#### APPLICATION TO INYO CRATERS

The theoretical and physical models suggest the following idealized sequence for surface deformation above a shallow dike such as that proposed for Inyo craters (Figure 16). In Figure 16a, vertical fractures and perhaps other forms of inelastic deformation develop around the dike top in the subsurface. In addition, two gentle topographic highs corresponding to subsurface anticlines and two zones of extensional strain develop at the surface on opposite sides of the dike plane. If the stratigraphy contains alternating rock layers with different mechanical properties, extensional fractures are likely to be concentrated in one set of layers (stippled in Figure 16), and shearing may be concentrated in another (unstippled). At Inyo craters, the extensional cracks may have been concentrated in the massive basalt flow units and shearing may have been concentrated in the interflow rubble units. In Figure 16b, fissures form at the surface on the inner slopes of the topographic highs. During the opening of these fissures, a contractional strain develops in the center of the trough directly above the dike. Fracturing continues in the subsurface above the dike top, and on the limbs of a gentle syncline that develops above the dike. In Figure 16c, additional fissures form, primarily inward toward the dike plane relative to the first fissures. The area between the innermost fissures is further compressed. In the experimental models, small thrust faults or pressure ridges form. At Inyo craters no such thrust faults are observed, possibly because the massive basalt flows in the subsurface are too strong in compression to produce thrust faults at this scale. Fracturing continues below the surface. In Figure 16d, fractures at depth connect with others in adjacent layers and with fissures at the surface. A graben develops above the dike due to dip-slip movement on some of the extensional fractures. Unbending of the surface directly above the dike may produce small extensional fractures within the graben.

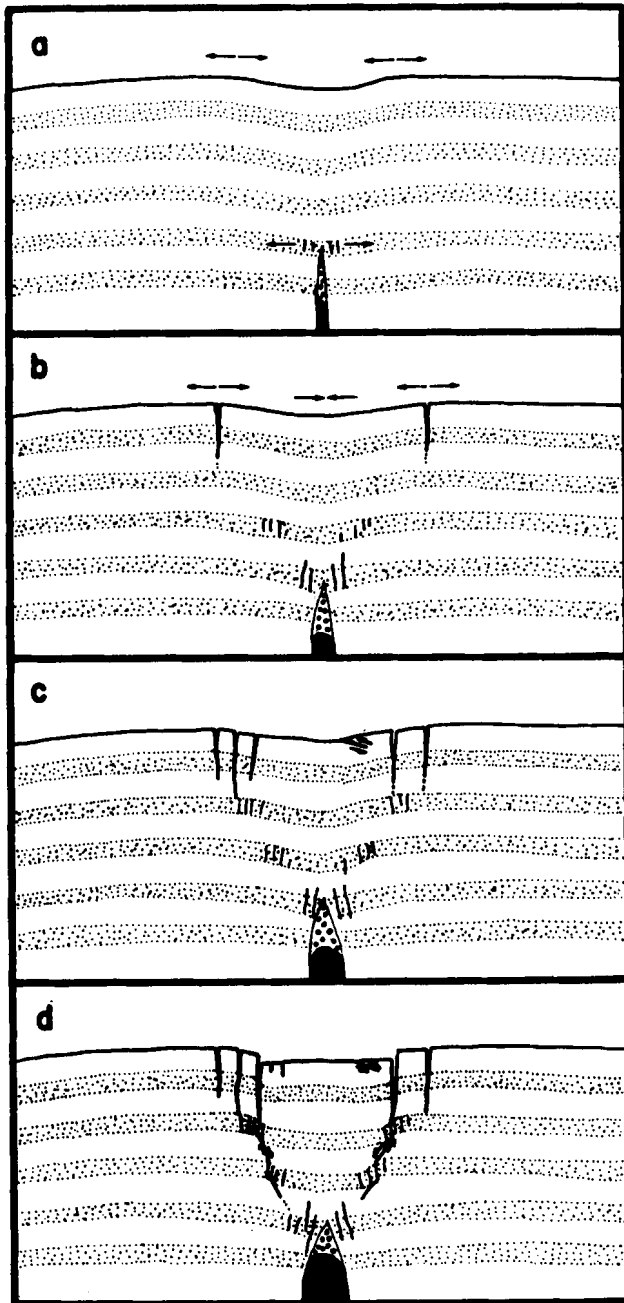


Fig. 16. Idealization of the sequence of fault and fissure growth above a shallow dike, based on results of the physical models. The stipple pattern denotes schematic marker beds similar to the corn meal layers in the experiments.

The theoretical models showed that the spacing between the outermost fissures south of south Inyo crater corresponds to the spacing between horizontal strain maxima predicted for a dike whose top is about 250 m deep. The results of the experimental modelling, however, suggest that the dike top could be up to several times this deep. Estimates of the east-west surface extension south of south Inyo crater (10 m to several tens of meters), in conjunction with ratios (0.59–0.73) of the surface extension to average dike thickness  $t_d$  measured in the experiments (Figure 14), suggest that the dike thickness at Inyo craters may range from about 14 m to about 100 m. The upper limit of this range is considerably

less than the estimate (a few hundred meters) based on ratios of surface extension to  $t_d$  calculated from elastic models. The experimental observation that fissures first form at the surface when  $t_d/d$  approaches 0.08 to 0.10 suggests that the dike may have been a few hundred meters to perhaps a kilometer deep when surface deformation began at Inyo craters.

The flow of water and steam ahead of the dike top has not been considered in this model but would be expected to increase both pore pressures and hydraulic fracturing pressures in the host rock and would therefore promote the growth of fractures immediately above the dike top. The phreatic eruptions leading to crater development presumably began as these fractures breached the surface. This process may be partly responsible for the fact that the Inyo craters lie within the graben, rather than along the bounding faults.

The experimental and numerical models both consider only a stationary dike top. Upward propagation of the dike top would promote the growth of additional new fissures inward toward the dike plane. In addition, the lower parts of faults that formed when the dike was at a certain depth might have become locked as the dike top ascended [as suggested by Rubin and Pollard, 1988]. This process could promote the growth of new normal faults inboard of the older ones.

#### DRILLING RESULTS AND IMPLICATIONS

During the course of this research, two holes were drilled within a kilometer of the Inyo craters. One hole, named IDFU 44-16 and drilled by Unocal Geothermal Division [Suenicht, 1987], was sited 700 m east-southeast of south Inyo crater (Figure 1) at an elevation about 70 m below the crater rim. The hole is 1799 m deep and is within a few degrees of vertical over its entire length. It encountered the following stratigraphy (from top to bottom): 378 m of basalt and interbedded sediments, 537 m of early post-caldera rhyolite lava and tuff, 253 m of Bishop Tuff, and 475 m of Tertiary dacites and andesites. Metamorphic basement rocks of calc-silicate hornfels were encountered at a depth of 1634 m.

A second hole, Inyo 4, was drilled with funding from the Department of Energy, Office of Basic Energy Sciences. Results of the drilling project are presented by Eichelberger *et al.* [1988]. This hole was sited 216 m southwest of the center of south Inyo crater at an elevation approximately 15 m above the crater rim (Figure 2). The hole was slanted toward the center of the crater, passed directly under the crater center at a vertical depth of 566 m, and terminated 79 m northeast of the crater center at a depth of 810 m. The hole encountered (from top to bottom) 319 vertical meters of basalt, 54 m of gravels, 342 m of early post-caldera rhyolite, 62 m of clastic deposits which may represent a glacial till, and metamorphic basement of quartzite and hypabyssal intrusive rocks at 779 m vertical depth.

Inyo 4 encountered metamorphic basement at an elevation 900 m shallower than that at Unocal hole IDFU 44-16. In addition, although a total of 719 m of Bishop Tuff and Tertiary dacites and andesites were encountered in IDFU 44-16, no such units were cored in Inyo 4. The difference in stratigraphy suggests either (1) that a major east-side-down normal fault lies between these two wells and that the Bishop Tuff and Tertiary volcanic rocks were either not deposited or were eroded away west of the faults, or (2) that the metamorphic rock encountered at Inyo 4 represents

a block of basement that slumped from the caldera wall during or shortly after subsidence of the caldera.

The Inyo 4 hole encountered no intact dike in the subsurface. However, it did encounter three breccia bodies between 527 m and 642 m vertical depth. The breccias are not horizontal stratigraphic layers as they contain clasts from stratigraphically higher units [Eichelberger *et al.*, 1988]. When projected up to the surface these breccias lie within 25 m horizontally of the crater center. If the breccias are vertical north-south-trending tabular bodies, their cumulative thickness is approximately 20 m [Eichelberger *et al.*, 1988]. The breccias contain mostly clasts of early post-caldera rhyolite and metamorphic fragments from the wallrock. In addition, some glassy vesicular rhyolite fragments with unvesiculated margins (suggesting possibly chilling) make up at least 10% of the breccias [Eichelberger *et al.*, 1988]. These fragments are chemically distinct from all other rhyolites in the wallrock and may be a juvenile component derived from a deeper magma body [Eichelberger *et al.*, 1988].

If the breccias are related to the development of the Inyo craters, they may include both debris that fell back into the vent during the south Inyo crater eruption and debris that intruded and dilated a subsurface crack. The intrusion of breccia and steam in a crack would have produced a mechanical deformation field in the host rock which was similar to that around a dilating dike. It is not known how the present thickness of the breccia bodies encountered in the drill core might relate to the thickness of a breccia-filled crack at the time when the faults and fissures were forming. However the present combined thickness of the three breccia bodies (approximately 20 m) is near the low end of the thickness (14 m to perhaps 100 m) required to produce the surface extension south of south Inyo crater.

Alternatively, the surface deformation may have been produced by a dike which is deeper than the breccias encountered in the borehole. The evidence for juvenile debris in the breccias supports this hypothesis. By analogy with the experimental models, the lower part of the hole may have passed through the inelastic process zone above the dike top.

The difference in stratigraphy between the two holes raises the possibility that some or all of the surface deformation around the craters is simply the expression of a large subsurface normal fault. Detailed descriptions of the surface expressions of normal faults [e.g. Wallace, 1977], however, indicate that they generally consist of single, well-defined scarps with few, if any, open fissures. The nested graben structure around the craters and the abundance of open fissures south of south Inyo crater are more typical of surface deformation patterns above shallow dikes than the surface expressions of normal fault scarps.

#### APPENDIX: ELASTIC MODELS APPLIED TO FLOUR-SUGAR EXPERIMENTS

To model the surface strains above the linoleum sleeve in the flour-sugar experiments, a two-dimensional boundary element model for elastic deformation (named "TWODD"), written by Crouch and Starfield [1983], was used. This program has the advantage over the program used to model dike intrusion (outlined by Pollard and Holzhausen [1979]) in that it allows us to prescribe boundary conditions in

terms of normal or shear displacements ( $d_n$  and  $d_s$ ) as well as normal or shear stresses ( $\sigma_n$  and  $\sigma_s$ ). The boundary conditions used to model the experimental setup are as follows: on the free surface,  $\sigma_n = \sigma_s = 0$ ; on the sides of the linoleum sleeve,  $d_s = 0$  and  $d_n$  is as measured in the experiments; at the base of the box,  $d_n = 0$  and  $d_s$  has a magnitude of  $t_{\max}/2$  (where  $t_{\max}$  is the thickness of the linoleum sleeve at the base of the sleeve), directed away from the linoleum sleeve; at the box ends where the flour-sugar mixture contacts the polyurethane cushions, no boundary conditions are imposed. In Figure 14, stage 2, the opening displacements used to model the linoleum sleeve were obtained by measuring the sleeve thickness at 1-cm intervals from the top to the bottom of the sleeve on both sides of the box.

For the linoleum sleeve experiments illustrated in Figure 15, the opening displacement of the linoleum sleeve was measured at 1-cm increments over the height of the sleeve, and each opening displacement measurement was normalized to the opening displacement at the bottom of the box. An upper and lower bound for  $s_e$  (shaded region, Figure 15) reflects sleeve profiles whose normalized thickness at a given point is one standard deviation greater and less than the average measurement, respectively. The same program and external boundary conditions were used to model the second set of experiments, but a constant opening mode displacement was specified over the height of the vertical slot (Figure 15, heavy solid curve).

We have considered the possibility that the discrepancy between the experimental and theoretical results in Figure 15 is due to some discrepancy between the boundary conditions in the experimental setup and those in our model. Therefore three variations in experimental boundary conditions were considered to determine whether they could have produced a decrease in  $s_e$ : (1) an upward shear displacement imposed on the linoleum walls during insertion of the cardboard strips, (2) a boundary condition of zero normal displacement at the polyurethane cushions at the ends of the box, and (3) friction along the plexiglass faces of the box. Numerical models of the first two variations show that they do not significantly affect  $s_e$ . Friction along the plexiglass sides of the box cause the cracks to visibly splay outward away from the centerline near the box ends, but this effect is visible and is significant only within a few centimeters of the box ends.

**Acknowledgments.** This research has been supported by the Department of Energy, Office of Basic Energy Sciences, under grant DE-FG03-85ER13319 as part of the Continental Scientific Drilling Program. The drilling team from Sandia Laboratories, especially John Eichelberger, made this study possible and provided us with many helpful comments regarding the origin of structures at Inyo craters. Thoughtful reviews by Roy Bailey, John Eichelberger, Gail Mahood, and Jian Lin have improved this paper considerably. Discussions with Allan Rubin, relating to his work on dike-induced surface deformation in Iceland and Hawaii, have added considerable insight. Bob Enriken and Steve Martel graciously helped survey profiles.

#### REFERENCES

- Bailey, R. A., G. B. Dalrymple, and M. A. Lanphere, Volcanism, structure, and geochronology of the Long Valley caldera, Mono County, California, *J. Geophys. Res.*, **81**, 725-744, 1976.
- Broek, D., *Elementary Engineering Fracture Mechanics*, 469 pp., Martinus Nijhoff, 1982.

- Castle, R. O., J. E. Estrem, and J. C. Savage, Uplift across Long Valley caldera, California, *J. Geophys. Res.*, **89**, 11,507-11,516, 1984.
- Cloos, E., Experimental analysis of fracture patterns, *Geol. Soc. Am. Bull.*, **66**, 241-256, 1955.
- Cloos, E., Experimental analysis of Gulf Coast fracture patterns, *Am. Assoc. Pet. Geol. Bull.*, **52**, 420-444, 1968.
- Cloos, H., Hebung, Spaltung, Vulkanismus, *Geol. Rundsch.*, **30**, 405-527, 1939.
- Crouch, S. L., and A. M. Starfield, *Boundary Element Methods in Solid Mechanics*, 322 pp., Allen and Unwin, Winchester, Mass., 1983.
- Delaney, P. T., D. D. Pollard, J. I. Ziony, and E. H. McKee, Field relations between dikes and joints: Emplacement processes and paleostress analysis, *J. Geophys. Res.*, **91**, 4920-4938, 1986.
- Eichelberger, J. C., P. C. Lysne, C. D. Miller, and L. W. Younker, Research drilling at Inyo domes, California: 1984 results, *Eos Trans. AGU*, **66**, 186-187, 1985.
- Eichelberger, J. C., T. A. Vogel, L. W. Younker, C. D. Miller, G. H. Heiken, and K. H. Wohletz, Structure and stratigraphy beneath a young phreatic vent, south Inyo crater, Long Valley caldera, California, *J. Geophys. Res.*, this issue.
- Fink, J. H., Geometry of silicic dikes beneath the Inyo domes, California, *J. Geophys. Res.*, **90**, 11,127-11,134, 1985.
- Fink, J. H., and D. D. Pollard, Structural evidence for dikes beneath silicic domes, Medicine Lake Highland Volcano, California, *Geology*, **11**, 458-461, 1983.
- Hill, D. P., R. A. Bailey, and A. S. Ryall, Active tectonic and magmatic processes beneath Long Valley caldera, eastern California: An overview, *J. Geophys. Res.*, **90**, 11,111-11,120, 1985.
- Horsfield, W. T., An experimental approach to basement controlled faulting, *Geol. Mijnbouw*, **56**, 363-370, 1977.
- Horsfield, W. T., Contemporaneous movement along crossing conjugate normal faults, *J. Struct. Geol.*, **2**, 305-310, 1980.
- Hubbert, M. K., Theory of scale models as applied to the study of geologic structures, *Geol. Soc. Am. Bull.*, **48**, 1459-1520, 1937.
- Huber, N. K., and C. D. Rinehart, Cenezoic volcanic rocks of the Devil's Postpile Quadrangle, eastern Sierra Nevada, California, *U. S. Geol. Surv. Prof. Pap.* 554-D, D1-D21, 1967.
- Irwin, G. R., J. A. Kies, and H. L. Smith, Fracture strengths relative to onset and arrest of crack propagation, *Proc. Am. Soc. Test. Mater.* **58**, 640-657, 1958.
- Metz, J. M., and G. A. Mahood, Precursors to the Bishop Tuff eruption: Glass Mountain, Long Valley, California, *J. Geophys. Res.*, **90**, 11,121-11,126, 1985.
- Miller, C. D., Holocene eruptions at the Inyo volcanic chain, California: Implications for possible eruptions in Long Valley caldera, *Geology*, **3**, 14-17, 1985.
- Murray, J. B., and A. D. Pullen, Three-dimensional model of the feeder conduit of the 1983 eruption of Mt. Etna Volcano, from ground deformation measurements, *Bull. Volcanol.*, **47-4**, 1145-1163, 1984.
- Oertel, G., The mechanism of faulting in clay experiments, *Tectonophysics*, **2**, 343-393, 1965.
- Pollard, D. D., Elementary fracture mechanics applied to the structural interpretation of dykes: Mafic Dyke Swarms, edited by H. C. Halls and W. F. Fahrig, *Spec. Pap. Geol. Assoc. Can.* **34**, 5-24, 1988.
- Pollard, D. D., and G. Holzhausen, On the mechanical interaction between a fluid-filled fracture and the Earth's surface, *Tectonophysics*, **53**, 27-57, 1979.
- Pollard, D. D., P. T. Delaney, W. A. Duffield, E. T. Endo, and A. T. Okamura, Surface deformation in volcanic rift zones, *Tectonophysics*, **94**, 541-584, 1983.
- Pollard, D. D., J. H. Fink, and P. T. Delaney, Igneous dikes at Long Valley, CA: Emplacement mechanisms and associated geologic structures, *U.S. Geol. Surv. Open File Rep.*, **84-939**, 130-146, 1984.
- Rinehart, C. D., and N. K. Huber, The Inyo Crater Lakes--A blast in the past, *Calif. Div. Mines Geol. Miner. Inf. Service Bull.*, **18**, 169-172, 1965.
- Rubin, A. M., and D. D. Pollard, Dike-induced rift zones in Iceland and Afar, *Geology*, **16**, 413-417, 1988.
- Savage, J. C., and M. M. Clark, Magmatic resurgence in Long Valley caldera, California: Possible cause of the 1980 Mammoth Lakes earthquakes, *Science*, **217**, 531-533, 1982.
- Sigurdsson, O., Surface deformation of the Krafla Fissure Swarm in two rifting events, *J. Geophys.*, **47**, 154-159, 1980.
- Suermann, G., Results of deep drilling in the western moat of Long Valley, California, *Eos Trans. AGU*, **68**, 785, 1987.
- Wallace, R. E., Profiles and ages of young fault scarps, north-central Nevada, *Geol. Soc. Am. Bull.*, **88**, 1267-1281, 1977.
- Wood, S. H., Distribution, correlation, and radiocarbon dating of late Holocene tephra, Mono and Inyo craters, eastern California, *Geol. Soc. Am. Bull.*, **88**, 89-95, 1977.

L. G. Mastin, and D. D. Pollard, Department of Applied Earth Sciences, Stanford University, Stanford, CA 94305

(Received September 14, 1987;  
revised February 10, 1988  
accepted March 9, 1988)